

AuCu nanofibers for electrosynthesis of urea from carbon dioxide and nitrite

Songliang Liu

Zhejiang University of Technology

Shuli Yin

Zhejiang University of Technology

Ziqiang Wang

Zhejiang University of Technology

You Xu

Zhejiang University of Technology

Xiaonian Li

Zhejiang University of Technology

Liang Wang

Zhejiang University of Technology

Hongjing Wang (✉ hjw@zjut.edu.cn)

Zhejiang University of Technology

Article

Keywords: AuCu nanofibers, electrocatalysis, urea synthesis, carbon dioxide reduction reaction, nitrite reduction

Posted Date: September 29th, 2021

DOI: <https://doi.org/10.21203/rs.3.rs-940285/v1>

License:   This work is licensed under a Creative Commons Attribution 4.0 International License.

[Read Full License](#)

Abstract

Carbon dioxide reduction reaction (CO₂RR) is a promising technology for mitigating greenhouse gas emission and achieving carbon neutrality. However, coupling CO₂RR with other reactions to produce high value-added chemicals remains a challenge. In this work, we report self-assembled nanofibers composed of ultra-thin AuCu alloy nanowires possessing a Boerdijk-Coxeter structure with (111)-dominant facets for the electrosynthesis of urea by coupling CO₂RR with nitrite reduction reaction (NO₂⁻RR). The rich structural defects and AuCu bimetallic alloy composition provide a large number of highly catalytically active sites. The constructed AuCu nanofibers display excellent urea synthesis performance in the electrolyte solution containing 0.01 M KNO₂ with continuous drumming of CO₂, achieving a high urea yield rate of up to 3889.6 μg h⁻¹ mg⁻¹_{cat.} and a high Faraday efficiency of 24.7% at -0.9 V. This work provides a feasible method for the rational design of self-assembled bimetallic nanofibers for electrosynthesis of urea under ambient conditions.

1. Introduction

Carbon dioxide (CO₂) is one of the main gases that contribute to the greenhouse effect.¹⁻⁵ With the rapid consumption of fossil fuels, CO₂ emissions will continue to increase.⁶⁻⁸ In addition, due to the intervention of anthropogenic activities (industrial production emissions, over-fertilization), large amounts of nitrogen pollutants (nitrite (NO₂⁻) and nitrate (NO₃⁻)) enter the ground to pollute water sources and pose a potential threat to the environment and human health.⁹⁻¹³ Therefore, the simultaneous reduction of CO₂ and NO_x⁻ to high value-added products is a renewable and economical promising approach.

Urea (CO(NH₂)₂) is an essential source of nitrogen for fertilizers and is widely applied as raw material for pesticides and medicines.¹⁴⁻¹⁶ However, the traditional method of synthesizing urea requires to be carried out under harsh conditions of high temperature and pressure and consumes large amounts of fossil fuels.^{17,18} Therefore, much effort has been devoted to explore green and sustainable strategies for urea synthesis.¹⁹⁻²¹ Recently, Wang and co-authors prepared urea by electrochemical method coupling the N₂ reduction reaction with the CO₂ reduction reaction (CO₂RR).²² Nevertheless, the limited solubility of N₂ in water and the high activation energy barrier of N≡N lead to a low urea yield rate (r_{urea}) and the corresponding poor Faraday efficiency (FE). Compared with N₂, the high solubility of NO₂⁻ in water and its low activation energy barrier make the utilization of NO₂⁻ as a nitrogen source for electrochemical reduction reaction coupled with CO₂RR to produce urea is more attractive.²³ For instance, Zhang and co-authors synthesized urea by coupling CO₂RR with NO₂⁻ reduction reaction (NO₂⁻RR) on oxygen vacancy-rich ZnO porous nanosheets.²⁴ However, this strategy has parallel CO₂RR and the NO₂⁻RR, which will generate complex product distribution, thus reducing the FE of the urea and increasing the difficulty of separating urea from the product.^{25,26} Therefore, the design and construction of electrocatalysts with high catalytic activity and selectivity are essential for the electrochemical synthesis of urea.

Cu-based catalysts have been proven to be highly efficient electrocatalysts for driving CO₂RR and NO₂⁻RR, but achieving highly selective synthesis of urea remains challenging.²⁷⁻³² The design and preparation of Cu-based catalysts with unique morphology, structure, and composition is a feasible approach to significantly improve catalytic activity and selectivity.³³⁻³⁸ Considering from the aspect of compositional engineering, alloying Cu with Au or other metals with high CO selectivity to CO₂RR could change the coordination structure and electronic structure of Cu atoms, enhance the adsorption and activation of CO₂, and increase the catalytic selectivity to reduce the types of products.³⁹⁻⁴¹ From the perspective of structural design, one-dimensional (1D) nanoarchitectures have unique structural features such as anisotropy, high flexibility, high aspect ratio, and low aggregation, etc., which have wide applications in the field of electrocatalysis.⁴²⁻⁴⁶ Among them, the construction of self-assembled nanofibers by ultrafine 1D nanowires could provide a large surface area, a large number of exposed surface atomic active sites and excellent electron transport capacity. Despite the effort has been devoted to the self-assembly of nanowire, until now there has been no simple and effective method to self-assemble nanowires into nanofibers.^{47,48} Based on the above considerations, it is highly desired to develop an effective strategy to prepare AuCu alloyed nanofibrous catalysts for electrocatalytic coupling of urea synthesis.

In this work, we successfully fabricate a novel type of AuCu self-assembled nanofibers (AuCu SANFs) for the electrosynthesis of urea by coupling CO₂RR with NO₂⁻RR. With the assistance of 4-aminopyridine, AuCu nanofibers are self-assembled from AuCu ultrafine nanowires with (111)-dominant facets and Boerdijk-Coxeter structure. When used for electrochemical urea production, the prepared AuCu SANFs exhibit excellent r_{urea} (3889.6 $\mu\text{g h}^{-1} \text{mg}^{-1}_{\text{cat}}$) and high FE (24.7%) in electrolyte with continuous drumming of CO₂. The excellent urea synthesis activity and stability of AuCu SANFs could be attributed to the 1D parallel nanowire fibrous structure and AuCu bimetallic composition. This work provides an effective strategy for the simple preparation of nanofibrous structure and expands the application of CO₂RR to successfully prepare urea with high added value.

2. Results

2.1 Materials characterization

The preparation process of the AuCu SANFs is illustrated in Scheme 1. AuCu SANFs are self-assembled from ultrathin AuCu alloy nanowires (AuCu NWs) with the assistance of 4-aminopyridine in a water bath at 20°C. The morphology and microstructural of the AuCu SANFs are investigated by scanning electron microscopy (SEM), high-angle annular dark-field scanning TEM (HAADF-STEM) and transmission electron microscopy (TEM). The typical SEM image of the AuCu SANFs displays a 1D curved nanofibers architecture with a high yield (Fig. 1a). HAADF-STEM and TEM images further confirm the formation of uniform anisotropic nanofibrous structures, consistent with the SEM observation results (Figs. 1b and 1c). Focusing on a single 1D nanofiber it can be clearly observed that a nanofiber is self-assembled from

numerous ultrathin nanowires parallel to each other (Fig. 1d). As revealed by the HAADF-STEM image and the corresponding energy dispersive X-ray (EDX) elemental mapping, Au and Cu elements are uniformly distributed in the nanofibers, supporting the formation of AuCu alloys (Fig. 1e-1f). The EDX analysis of AuCu SANFs indicates the atomic ratio of Au/Cu is approximately 1/1 (Fig. S1).

The selected area electron diffraction (SAED) pattern strongly evidences the polycrystalline features of the AuCu SANFs (Fig. 2a). The high-resolution TEM (HRTEM) images show an average diameter of 2.71 ± 0.02 nm for the individual nanowire with the lattice spacing (0.236 nm) is indexed to the (111) plane of face-centered-cubic (fcc) AuCu alloy (Figs. 2b and 2c). Moreover, a representative set of HRTEM images of the individual AuCu NW further reveal the domains of nanocrystal facets along the longitudinal direction of the nanowire (Figs. 2d-2f). The average value of the lattice stripe spacing from the different domains of AuCu NW is about 0.236 nm. Furthermore, AuCu NWs exhibit abundant twin boundaries (red arrows), stacking faults (blue arrows) and atomic steps (circles), which could be used as high catalysis active sites (Figs. 2d-2f).⁴⁹⁻⁵¹ More importantly, the individual AuCu NWs that make up the nanofibers are all Boerdijk-Coxeter type helix (Fig. 2g) and mostly terminated by (111)-type planes. The obtained Boerdijk-Coxeter type helix of AuCu NWs are similar to the helix that appears in Au⁵², AuPt⁴⁷ and AuAg⁵³ nanowires.

The X-ray diffraction (XRD) pattern is employed to investigate the crystal structure of the prepared nanofibers. The XRD pattern of AuCu SANFs exhibits typical diffraction peaks of the metallic fcc structure (Fig. S2). It is noteworthy that the diffraction peaks of AuCu SANFs in the XRD pattern are located between the diffraction peaks of standard fcc Au (JCPDS-65-8601) and Cu (JCPDS-04-0836), further indicating the formation of AuCu alloys. The surface electronic states and the chemical composition of AuCu SANFs are further investigated by X-ray photoelectron spectroscopy (XPS). In the XPS spectrum of Au 4f, the typical peaks with binding energies at 87.4 eV could be indexed to Au 4f_{5/2}, while that at 83.7 eV could be indexed to Au 4f_{7/2} (Fig. 3a). In the high-resolution Cu 2p XPS spectrum, two major peaks at 951.3 eV and 931.6 eV could be assigned to Cu(0) 2p_{1/2} and Cu(0) 2p_{3/2}, respectively (Fig. 3b). The observed a low content of Cu(II) species appearing at 953.7 eV and 933.8 eV are attributed to Cu(II) 2p_{1/2} and Cu(II) 2p_{3/2}, probably owing to the oxidation of AuCu SANFs in air.^{40,54} In addition, the peaks located at 962.1 eV and 942.5 eV could be corresponding to the satellite peaks of Cu 2p_{1/2} and Cu 2p_{3/2}, respectively.

A series of controlled experiments are carried out to explore the mechanism of the formation of AuCu SANFs. In the absence of 4-aminopyridine, irregularly agglomerated nanoparticles are formed, while the excess of 4-aminopyridine causes the nanofibers to stack together (Fig. S3). 4-Aminopyridine acts as a structure-directing agent in the synthesis system, and appropriate amount of 4-aminopyridine is essential for the successful preparation of nanofibers. Replacing 4-aminopyridine with other structure-directing agents (F127, DM970, PVP, CTAB) fails to form unique nanofibers (Fig. S4). As shown in Fig. S5, when AA is replaced with more reductive reagents, the faster reduction rates lead to the formation of bimetallic AuCu alloys with 1D nanowire structures. Nanowires with uneven thickness are obtained by using N₂H₄

as a reducing agent (Fig. S5a). HCOOH as a reducing agent turns the prepared AuCu SANFs into a mixture of nanoparticles and nanowires (Fig. S5b). The worm-like nanowires are obtained using the more reducing NaBH_4 (Fig. S5c). These results indicate that the choice of AA with moderate reducing kinetics as a reducing agent is crucial for the formation of AuCu SANFs. Interestingly, we find that controlling the reaction temperature could achieve self-assembly and disassembly of nanofibers (Fig. S6). With the gradual increase of the reaction temperature, the nanofibers are gradually disassembled. When the temperature is increased to 100°C , the nanofibers are completely disassembled into uniform 1D ultrafine nanowires (Fig. S6f). The results reveal that lower reaction temperature could slow down the reduction ability of AA, which is more favorable to the formation of AuCu SANFs.

The potential formation mechanism of AuCu SANFs could be acquired from the results of the above research. First, the metal precursors (HAuCl_4 , CuCl_2) are rapidly adsorbed by 4-aminopyridine at 20°C . After the addition of AA, the precursors are slowly reduced to Au and Cu atoms. As the reaction progresses, the metal atoms form AuCu cores through Ostwald maturation assembly, which reduces the total surface free energy in the system.^{55,56} Then, with the assistance of 4-aminopyridine, ultrafine AuCu NWs are formed by anisotropic epitaxial growth. Final, in order to minimize the total surface free energy, the ultrafine AuCu NWs with abundant structural defects undergo strong cohesive interactions when in contact with each other and further self-assemble into AuCu SANFs under the constraint of 4-aminopyridine.⁴⁷

2.2 Electrocatalytic performances for CO_2RR

AuCu SANFs were conducive to the adsorption and activation of the CO_2 , NO_2^- species due to their 1D self-assembled nanofiber structure and the synergistic effects between Au and Cu elements.^{30,39,57} Urea electrosynthesis by coupling CO_2RR with $\text{NO}_2^- \text{RR}$ was evaluated by the potentiostatic method using H-type electrolytic cells at ambient temperature and pressure (Fig. S7). First, the CO_2RR and $\text{NO}_2^- \text{RR}$ properties of AuCu SANFs were investigated. Figure 4a shows the LSV curves of AuCu SANFs measured in Ar-saturated and CO_2 -saturated 0.5 M KHCO_3 solutions. It is obvious that the specific current densities of AuCu SANFs in CO_2 -saturated 0.5 M KHCO_3 solution is much higher than that in Ar-saturated 0.5 M KHCO_3 solution, indicating that an effective electrocatalytic CO_2RR occurs on AuCu SANFs. Then, CO_2 is passed into the 0.5 M KHCO_3 solution at a flow rate of 20 mL min^{-1} and electrolyzed at the selected potential. All the curves have no significantly change, indicating that the AuCu SANFs possess excellent catalytic stability for CO_2RR (Fig. S8). As shown in Fig. 4b, CO is the main product of CO_2 reduction occurring on AuCu SANFs, and the FE of CO (89.5%) reaches highest at -0.6 V . As the potential continues to decrease, the FE of CO significantly decreases due to the enhancement of the competing hydrogen evolution reaction (HER). The partial current density corresponding to CO reaches -3.8 mA cm^{-2} at -0.6 V and the H_2 partial current density is -0.4 mA cm^{-2} , resulting in the FE of H_2 only 10.5%, indicating the AuCu SANFs have efficient electrocatalytic reduction activity and selectivity for the conversion of CO_2 to CO (Figs. 4c and S9). The stability of the CO_2 reduction for AuCu SANFs is investigated by long-term

chronoamperometric measurement at -0.6 V for 20 h. The current density only slightly decays and the FE of CO is almost unchanged, indicating that the AuCu SANFs still maintains high CO₂RR activity after long-term electrolysis (Fig. 4d).

2.3 Electrocatalytic performances for NO₂⁻RR

Subsequently, the NO₂⁻RR performance of the AuCu SANFs was investigated. Figure 5a shows the LSV curves in the absence and addition of 0.01 M KNO₂ in 0.5 M KHCO₃ solution. Compared to the electrolyte without NO₂⁻, the LSV curve in the presence of NO₂⁻ shows a more positive onset potential and a larger current density, indicating that the NO₂⁻RR occurs on the AuCu SANFs. Next, a chronoamperometry test is carried out at the selected potential for 2 h to evaluate the electrocatalytic NO₂⁻ performance of the AuCu SANFs (Fig. S10). The absorption intensities of the remaining NO₂⁻ and the generated NH₃ are measured using UV-Vis spectroscopy. The FE of NH₃, NH₃ yield rate (r_{NH_3}) and NH₃ selectivity at the corresponding potentials are calculated from the calibration curves (Figs. S11 and S12). The FE (78.7%) of NH₃ for AuCu SANFs reaches the highest value at -0.8 V, and the corresponding r_{NH_3} also reaches 5254.1 $\mu\text{g h}^{-1} \text{mg}^{-1}_{\text{cat}}$ (Figs. 5b and 5c). When the potential continues to decrease, the r_{NH_3} continues to increase, but the corresponding FE sharply decreases due to the competitive HER. In addition, the NH₃ selectivity of the AuCu SANFs reach 91%, and the by-product N₂ selectivity is only 9% (Fig. 5d).

2.4 Electrochemical performances of the urea production by coupling CO₂RR with NO₂⁻RR

The AuCu SANFs were further used as a catalyst for the preparation of urea by coupling CO₂RR with NO₂⁻RR. The CO₂ was continuously drummed into the 0.5 M KHCO₃ solution containing 0.01 M KNO₂. Figure 6a shows the LSV curves with and without CO₂, which observed that the AuCu SANFs have a significant current response to CO₂RR. The chronoamperometry test was carried out at selected different potentials for 2 h, and all the curves did not significantly change, and the current density maintained excellent stability (Fig. S13). The generated urea was decomposed into NH₃ by urease.^{23,25} The absorption intensity of NH₃ converted from urea was measured by UV-Vis spectrophotometry, and the concentration was further determined from the calibration curve (Fig. S14). The FE of urea for AuCu SANFs reached the highest of 24.7% and the corresponding r_{urea} was 3889.6 $\mu\text{g h}^{-1} \text{mg}^{-1}_{\text{cat}}$ at -0.9 V (Figs. 6b and 6c). It is comparable to the recently reported performance of ZnO-V porous nanosheets²⁴, lies between those of Te-Doped Pd Nanocrystal²³ and oxygen vacancy-rich anatase TiO₂²⁵. As the potential further decreases, the FE of urea decreases due to enhanced side reactions. At the optimum potential of -0.9 V, the FE of H₂, NH₃, N₂ and CO were 16.4%, 10.1%, 4.6% and 42.7%, respectively (Fig. 6d). The urea selectivity, by-product NH₃ selectivity and N₂ selectivity of the AuCu SANFs at -0.9 V were 62.7%, 25.5% and 11.8%, respectively (Fig. 6e). The electrocatalytic stability of the AuCu SANFs was evaluated

by performing five continuous cycles at -0.9 V. The FE of urea and r_{urea} remain almost unchanged after the cycles, indicating that the AuCu SANFs have excellent catalytic stability for the preparation of urea coupled by CO₂RR and NO₂⁻RR (Fig. 6f).

A series of comparative experiments were performed to further confirm that the urea generated originated from CO₂ reduction and NO₂⁻ reduction and to eliminate the influence of environmental or impurities in the reaction system on the measurement results (Figs. S15 and S16). As shown in Fig. S15, the FE of NH₃ and the FE of CO under the CO₂ + NO₂⁻ condition are lower than those under the NO₂⁻ condition and the CO₂ condition, respectively. Moreover, there is a significant difference in FE at -0.9 V, indicating that urea production probably is attributed to the consumption of CO and NH₃. Under various conditions, urea was produced only under CO₂ + NO₂⁻ conditions, indicating that the urea was indeed derived from both CO₂ reduction and NO₂⁻ reduction (Fig. S16). In addition, no urea was detected after replacing CO₂ with CO or NO₂⁻ with NH₄⁺, suggesting that urea formation originated from intermediates prior to the formation of CO and NH₃ (Fig. S16). Based on the above results, a possible mechanism of urea electrosynthesis was proposed (Fig. S17). CO₂ could be reduced to CO* intermediates (Eq. 1) and NO₂⁻ could be reduced to NH₂* precursors (Eq. 2) on the AuCu SANFs. Subsequently, the NH₂* precursors were coupled to the CO* intermediates via a tandem reaction pathway, thereby being converted into urea (Eq. 3).

AuCu SANFs exhibit enhanced electrocatalytic activity and excellent stability, which could be attributed to the following reasons: (1) AuCu SANFs are composed of unique 1D AuCu NWs arranged in parallel with anisotropic and high surface area characteristics, which enhance the utilization of Au atoms and Cu atoms, accelerate electron transport and could effectively avoid agglomeration and dissolution of catalysts. Furthermore, the 1D AuCu NWs constituting AuCu SANFs have a large number of structural defects (twin boundaries, stacking faults and atomic steps) acting as active centers for catalysis.^{49–51, 58} (2) AuCu SANFs have a Boerdijk-Coxeter structure with parallel bundles (111)-dominant facets in different orientations, which could generate lattice strain and modulate the electronic structure, thus contributing to enhanced electrocatalytic performance.^{47,59} (3) The bimetallic composition is also essential for the excellent electrocatalytic activity and stability of the AuCu SANFs. AuCu alloying could modulate the coordination state and electronic structure of Au and Cu^{39,40}, which facilitates the adsorption and activation of reactants (CO₂, NO₂⁻), thus promoting the electrocatalytic coupling to produce urea.

3. Discussion

In summary, AuCu SANFs with high-quality 1D nanofiber structure have been successfully prepared in 4-aminopyridine solution by a one-pot chemical reduction method and tested as an efficient catalyst for coupling CO₂RR with NO₂⁻RR to prepare urea. AuCu SANFs are self-assembled by Boerdijk-Coxeter structural AuCu alloy nanowires with (111)-dominant facets. Integrating the advantages of 1D rich defect structure, (111) facet dominance, and bimetallic composition synergistic enhancement effect, the

resultant AuCu SANFs achieve a r_{urea} of $3889.6 \mu\text{g h}^{-1} \text{mg}^{-1}_{\text{cat}}$ with a corresponding FE of 24.7% at -0.8 V and excellent stability. This work not only provides a feasible approach for constructing nanofiber structure, but also promotes the investigation of electrochemical synthesis of urea under environmental conditions.

4. Methods

4.1. Materials and chemicals

HAuCl₄, Pluronic F127 (PEO₁₀₀PPO₆₅PEO₁₀₀), Nafion solution (5 wt%) and Nafion 117 membrane were received from Sigma-Aldrich. CuCl₂, 4-aminopyridine, Poly(vinylpyrrolidone) (PVP, M_w = 58000), N₂H₄·H₂O, hexadecyl trimethyl ammonium bromide (CTAB), DM-970 ((C₂H₄O)_n·C₂₄H₄₂O·C₁₅H₂₄O), NaBH₄, KHCO₃, NH₄HCO₃, sodium hydroxide (NaOH), salicylic acid, trisodium citrate dihydrate, sodium hypochlorite solution (NaClO), sodium nitroprusside, p-aminobenzenesulfonamide, N-(1-Naphthyl) ethylenediamine dihydrochloride, and urease were ordered from Aladdin. HCl, HCOOH, phosphoric acid, and ethanol were purchased from Beijing Chemical Works.

4.2. Synthesis of the AuCu SANFs

First, 47 mg of 4-aminopyridine was ultrasonically dissolved in 7 mL of deionized water. Second, 1 mL of HAuCl₄ (20 mM) and 1 mL of CuCl₂ (20 mM) were quickly added to the above solution and placed in a water bath at 20 °C. Third, 1 mL of AA (0.1 M) was quickly injected into the mixed solution and left for 10 minutes. Finally, the product was cooled at room temperature and washed 3 times with water and ethanol alternately, and dried under vacuum at 60 °C.

Data availability

Source data to generate Figures and tables are available from the corresponding authors upon reasonable request.

Declarations

Acknowledgment

This work was financially supported by the National Natural Science Foundation of China (No. 21601154, 21776255, 21972126, 21978264, 21905250).

Author contributions

Wang L. and Wang H. supervised the project. Liu S. conceived the idea and designed the experiments. Liu S. and Yin S. wrote the manuscript. Yin S., Wang Z., Xu Y. and Li X. discussed the experiment results. All authors have given approval to the final version of the paper.

Competing interests

The authors declare no competing interests.

Additional information

Supplementary information

The online version contains supplementary material available at <https://doi.org/>.

Open Access

Open Access This article is licensed under a Creative Commons Attribution 4.0 International License, which permits use, sharing, adaptation, distribution and reproduction in any medium or format, as long as you give appropriate credit to the original author(s) and the source, provide a link to the Creative Commons license, and indicate if changes were made. The images or other third party material in this article are included in the article's Creative Commons license, unless indicated otherwise in a credit line to the material. If material is not included in the article's Creative Commons license and your intended use is not permitted by statutory regulation or exceeds the permitted use, you will need to obtain permission directly from the copyright holder. To view a copy of this license, visit <http://creativecommons.org/licenses/by/4.0/>.

References

1. Ren S, *et al.* Molecular electrocatalysts can mediate fast, selective CO₂ reduction in a flow cell. *Science* **365**, 367-369 (2019).
2. Zou J, *et al.* Hierarchical architectures of mesoporous Pd on highly ordered TiO₂ nanotube arrays for electrochemical CO₂ reduction. *J. Mater. Chem. A* **8**, 8041-8048 (2020).
3. Li L, *et al.* Stable, active CO₂ reduction to formate via redox-modulated stabilization of active sites. *Nat. Commun.* **12**, 5223 (2021).
4. Deng P, *et al.* Bismuth oxides with enhanced bismuth–oxygen structure for efficient electrochemical reduction of carbon dioxide to formate. *ACS Catal.* **10**, 743-750 (2019).
5. Lu KQ, *et al.* Rationally designed transition metal hydroxide nanosheet arrays on graphene for artificial CO₂ reduction. *Nat. Commun.* **11**, 5181 (2020).
6. Xing Y, *et al.* Crumpled ir nanosheets fully covered on porous carbon nanofibers for long-life rechargeable lithium-CO₂ batteries. *Adv. Mater.* **30**, 1803124 (2018).
7. Arandiyana H, *et al.* Highly Selective reduction of carbon dioxide to methane on novel mesoporous Rh catalysts. *ACS Appl. Mater. Interfaces* **10**, 24963-24968 (2018).

8. Monteiro MCO, Philips MF, Schouten KJP, Koper MTM. Efficiency and selectivity of CO₂ reduction to CO on gold gas diffusion electrodes in acidic media. *Nat. Commun.* **12**, 4943 (2021).
9. Xu Y, *et al.* Cooperativity of Cu and Pd active sites in CuPd aerogels enhances nitrate electroreduction to ammonia. *Chem. Commun.* **57**, 7525-7528 (2021).
10. Wang C, Zhou W, Sun Z, Wang Y, Zhang B, Yu Y. Integrated selective nitrite reduction to ammonia with tetrahydroisoquinoline semi-dehydrogenation over a vacancy-rich Ni bifunctional electrode. *J. Mater. Chem. A* **9**, 239-243 (2021).
11. Zeng Z, *et al.* Orbital coupling of hetero-diatomic nickel-iron site for bifunctional electrocatalysis of CO₂ reduction and oxygen evolution. *Nat. Commun.* **12**, 4088 (2021).
12. Ren T, *et al.* Concave-convex surface oxide layers over copper nanowires boost electrochemical nitrate-to-ammonia conversion. *Chem. Eng. J.* **426**, 130759 (2021).
13. Wang R, Wang Z, Xiang X, Zhang R, Shi X, Sun X. MnO₂ nanoarrays: an efficient catalyst electrode for nitrite electroreduction toward sensing and NH₃ synthesis applications. *Chem. Commun.* **54**, 10340-10342 (2018).
14. Lv C, *et al.* Selective electrocatalytic synthesis of urea with nitrate and carbon dioxide. *Nature Sustain.*, (2021).
15. Xu M, Jupp AR, Ong MSE, Burton KI, Chitnis SS, Stephan DW. Synthesis of urea derivatives from CO₂ and silylamines. *Angew. Chem., Int. Ed.* **58**, 5707-5711 (2019).
16. Barzagli F, Mani F, Peruzzini MJGc. From greenhouse gas to feedstock: formation of ammonium carbamate from CO₂ and NH₃ in organic solvents and its catalytic conversion into urea under mild conditions. **13**, 1267-1274 (2011).
17. Aresta M, Dibenedetto A, Angelini A. Catalysis for the valorization of exhaust carbon: from CO₂ to chemicals, materials, and fuels. technological use of CO₂. *Chem. Rev.* **114**, 1709-1742 (2014).
18. Jouny M, *et al.* Formation of carbon-nitrogen bonds in carbon monoxide electrolysis. *Nat. Chem.* **11**, 846-851 (2019).
19. Chen W, *et al.* Unveiling the electrooxidation of urea: intramolecular coupling of the N-N bond. *Angew. Chem., Int. Ed.* **60**, 7297-7307 (2021).
20. Yuan M, *et al.* Unveiling electrochemical urea synthesis by co-activation of CO₂ and N₂ with Mott-Schottky heterostructure catalysts. *Angew. Chem., Int. Ed.* **60**, 10910-10918 (2021).

21. Zhang Z, Guo L. Electrochemical reduction of CO₂ and N₂ to synthesize urea on metal-nitrogen-doped carbon catalysts: a theoretical study. *Dalton. Trans.* **50**, 11158-11166 (2021).
22. Chen C, *et al.* Coupling N₂ and CO₂ in H₂O to synthesize urea under ambient conditions. *Nat. Chem.* **12**, 717-724 (2020).
23. Feng Y, *et al.* Te-doped Pd nanocrystal for electrochemical urea production by efficiently coupling carbon dioxide reduction with nitrite reduction. *Nano Lett.* **20**, 8282-8289 (2020).
24. Meng N, Huang Y, Liu Y, Yu Y, Zhang B. Electrosynthesis of urea from nitrite and CO₂ over oxygen vacancy-rich ZnO porous nanosheets. *Cell Reports Physical Science* **2**, 100378 (2021).
25. Cao N, *et al.* Oxygen vacancies enhanced cooperative electrocatalytic reduction of carbon dioxide and nitrite ions to urea. *J. Colloid Interface Sci.* **577**, 109-114 (2020).
26. Siva P, Prabu P, Selvam M, Karthik S, Rajendran V. Electrocatalytic conversion of carbon dioxide to urea on nano-FeTiO₃ surface. *Ionics.* **23**, 1871-1878 (2017).
27. Zhang B, *et al.* Highly Electrocatalytic ethylene production from CO₂ on nanodeficient Cu nanosheets. *J. Am. Chem. Soc.* **142**, 13606-13613 (2020).
28. Pan J, *et al.* Hierarchical and ultrathin copper nanosheets synthesized via galvanic replacement for selective electrocatalytic carbon dioxide conversion to carbon monoxide. *Appl. Catal. B: Environ.* **255**, 117736 (2019).
29. Chen D, *et al.* Surface composition dominates the electrocatalytic reduction of CO₂ on ultrafine CuPd nanoalloys. *Carbon Energy* **2**, 443-451 (2020).
30. Lyu Z, *et al.* Controlling the Surface Oxidation of Cu nanowires improves their catalytic selectivity and stability toward C₂₊ Products in CO₂ Reduction. *Angew. Chem., Int. Ed.* **60**, 1909-1915 (2021).
31. Li H, *et al.* Cu_xIr_{1-x} nanoalloy catalysts achieve near 100% selectivity for aqueous nitrite reduction to NH₃. *ACS Catal.* **10**, 7915-7921 (2020).
32. Zhu T, *et al.* Single-atom Cu catalysts for enhanced electrocatalytic nitrate reduction with significant alleviation of nitrite production. *Small* **16**, e2004526 (2020).
33. Liang J, *et al.* High-efficiency electrochemical nitrite reduction to ammonium using a Cu₃P nanowire array under ambient conditions. *Green Chem.* **23**, 5487-5493 (2021).
34. Liu S, *et al.* Rational construction of Au₃Cu@Cu nanocages with porous core-shell heterostructured walls for enhanced electrocatalytic N₂ fixation. *J. Mater. Chem. A* **9**, 8372-8377 (2021).

35. Cen S-Y, *et al.* Eco-friendly one-pot aqueous synthesis of ultra-thin AuPdCu alloyed nanowire-like networks for highly sensitive immunoassay of creatine kinase-MB. *Sensors and Actuators B: Chemical* **333**, (2021).
36. Zheng L, Yang D, Chang R, Wang C, Zhang G, Sun S. Crack-tips enriched platinum-copper superlattice nanoflakes as highly efficient anode electrocatalysts for direct methanol fuel cells. *Nanoscale* **9**, 8918-8924 (2017).
37. Yu H, *et al.* Bimetallic Ag₃Cu porous networks for ambient electrolysis of nitrogen to ammonia. *J. Mater. Chem. A* **7**, 12526-12531 (2019).
38. Wang Y, Zhou W, Jia R, Yu Y, Zhang B. Unveiling the activity origin of a copper-based electrocatalyst for selective nitrate reduction to ammonia. *Angew. Chem., Int. Ed.* **59**, 5350-5354 (2020).
39. Kim D, *et al.* Electrochemical activation of CO₂ through atomic ordering transformations of AuCu nanoparticles. *J. Am. Chem. Soc.* **139**, 8329-8336 (2017).
40. Zhu W, *et al.* Formation of Enriched Vacancies for Enhanced CO₂ electrocatalytic reduction over AuCu alloys. *ACS Energy Lett.* **3**, 2144-2149 (2018).
41. Kauffman DR, *et al.* Selective Electrocatalytic Reduction of CO₂ into CO at small, thiol-capped Au/Cu nanoparticles. *J. Phys. Chem. C* **122**, 27991-28000 (2018).
42. Wang H, *et al.* Amorphous sulfur decorated gold nanowires as efficient electrocatalysts toward ambient ammonia synthesis. *ACS Sustainable Chem. Eng.* **7**, 19969-19974 (2019).
43. Wang J, Qiu X, Su K, Wang S, Li J, Tang Y. Breaking the lattice match of Pd on Au(111) nanowires: manipulating the island and epitaxial growth pathways to boost the oxygen reduction reactivity. *J. Mater. Chem. A* **8**, 19300-19308 (2020).
44. Hong X, *et al.* AuAg nanosheets assembled from ultrathin AuAg nanowires. *J. Am. Chem. Soc.* **137**, 1444-1447 (2015).
45. Li F, *et al.* From monometallic Au nanowires to trimetallic AuPtRh nanowires: interface control for the formic acid electrooxidation. *J. Mater. Chem. A* **6**, 17164-17170 (2018).
46. Wang H, *et al.* Metal–nonmetal one-dimensional electrocatalyst: AuPdP nanowires for ambient nitrogen reduction to ammonia. *ACS Sustainable Chem. Eng.* **7**, 15772-15777 (2019).
47. Chang F, *et al.* Composition tunability and (111)-dominant facets of ultrathin platinum-gold alloy nanowires toward enhanced electrocatalysis. *J. Am. Chem. Soc.* **138**, 12166-12175 (2016).
48. Xia BY, Wu HB, Yan Y, Lou XW, Wang X. Ultrathin and ultralong single-crystal platinum nanowire assemblies with highly stable electrocatalytic activity. *J. Am. Chem. Soc.* **135**, 9480-9485 (2013).

49. Zhao X, Zhao H, Sun J, Li G, Liu R. Blocking the defect sites on ultrathin Pt nanowires with Rh atoms to optimize the reaction path toward alcohol fuel oxidation. *Chinese Chemical Letters* **31**, 1782-1786 (2020).
50. Liu R, *et al.* Defect Sites in Ultrathin Pd nanowires facilitate the highly efficient electrochemical hydrodechlorination of pollutants by H*ads. *Environ. Sci. Technol.* **52**, 9992-10002 (2018).
51. Zhang RL, Feng JJ, Zhang L, Shi CG, Wang AJ. Ultrathin PdFePb nanowires: one-pot aqueous synthesis and efficient electrocatalysis for polyhydric alcohol oxidation reaction. *J. Colloid Interface Sci.* **555**, 276-283 (2019).
52. Zhu Y, *et al.* Chiral gold nanowires with Boerdijk-Coxeter-Bernal structure. *J. Am. Chem. Soc.* **136**, 12746-12752 (2014).
53. Velázquez-Salazar JJ, *et al.* Experimental evidence of icosahedral and decahedral packing in one-dimensional nanostructures. **5**, 6272-6278 (2011).
54. Qiao B, Zhu J, Liu Y, Chen Y, Fu G, Chen P. Facile synthesis of porous PdCu nanoboxes for efficient chromium(vi) reduction. *CrystEngComm* **21**, 3654-3659 (2019).
55. Duan JJ, *et al.* Porous dendritic PtRuPd nanospheres with enhanced catalytic activity and durability for ethylene glycol oxidation and oxygen reduction reactions. *J. Colloid Interface Sci.* **560**, 467-474 (2020).
56. Wang X-Y, Han Z, Duan J-J, Feng J-J, Huang H, Wang A-J. Facile construction of 3D hyperbranched PtRh nanoassemblies: a bifunctional electrocatalyst for hydrogen evolution and polyhydric alcohol oxidation reactions. *Int. J. Hydrog. Energy* **45**, 8433-8443 (2020).
57. Wada K, Hirata T, Hosokawa S, Iwamoto S, Inoue M. Effect of supports on Pd-Cu bimetallic catalysts for nitrate and nitrite reduction in water. *Catal. Today* **185**, 81-87 (2012).
58. Yu H, *et al.* Defect-rich porous palladium metallene for enhanced alkaline oxygen reduction electrocatalysis. *Angew. Chem., Int. Ed.* **60**, 12027-12031 (2021).
59. Jiang X, *et al.* Highly simple and rapid synthesis of ultrathin gold nanowires with (111)-dominant facets and enhanced electrocatalytic properties. *J. Mater. Chem. A* **6**, 17682-17687 (2018).

Figures

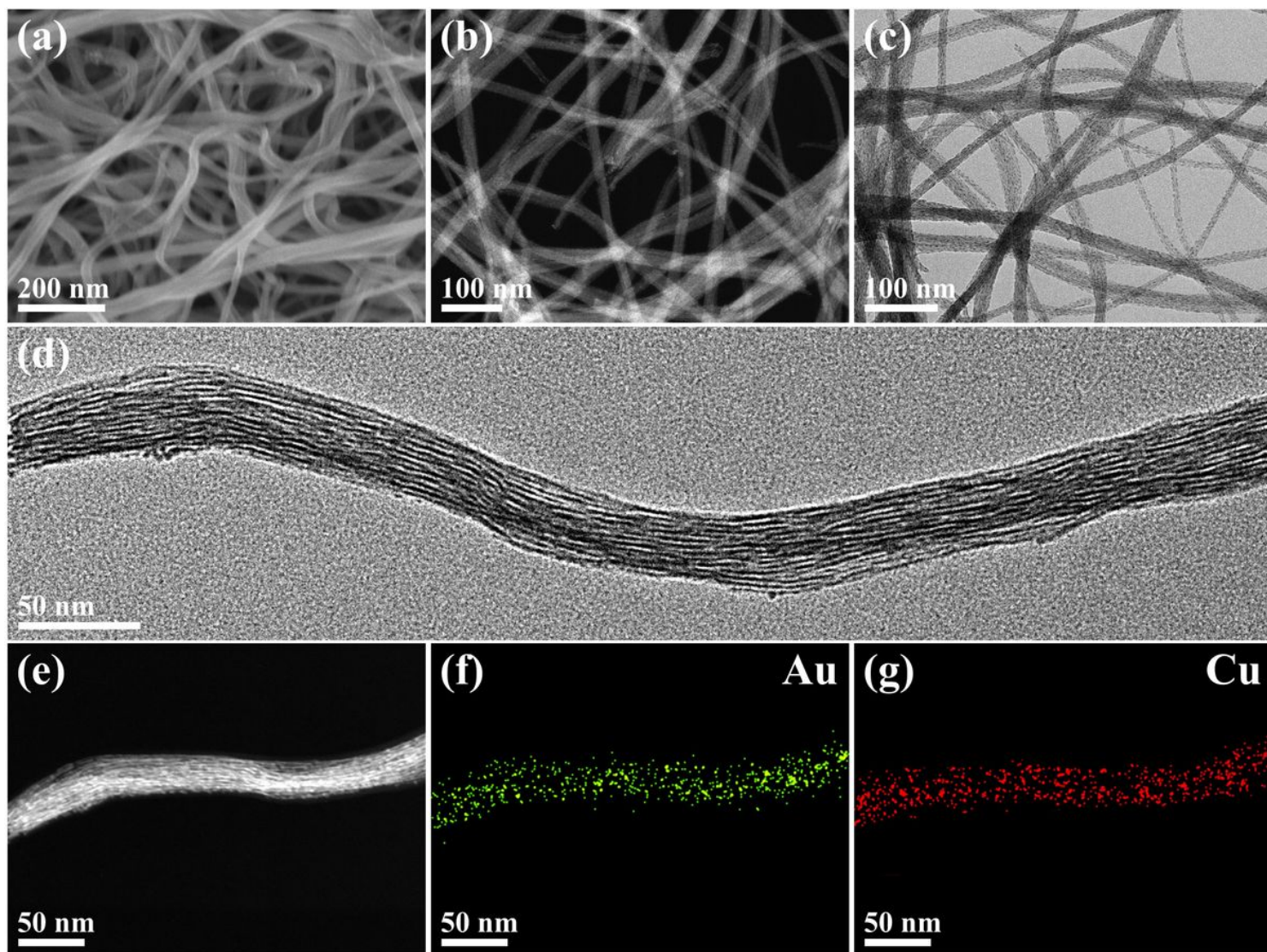


Figure 1

(a) SEM, (b) HAADF-STEM and (c and d) TEM images of the AuCu SANFs. (e) HAADF-STEM image and (f and g) EDS mapping images of the AuCu SANFs.

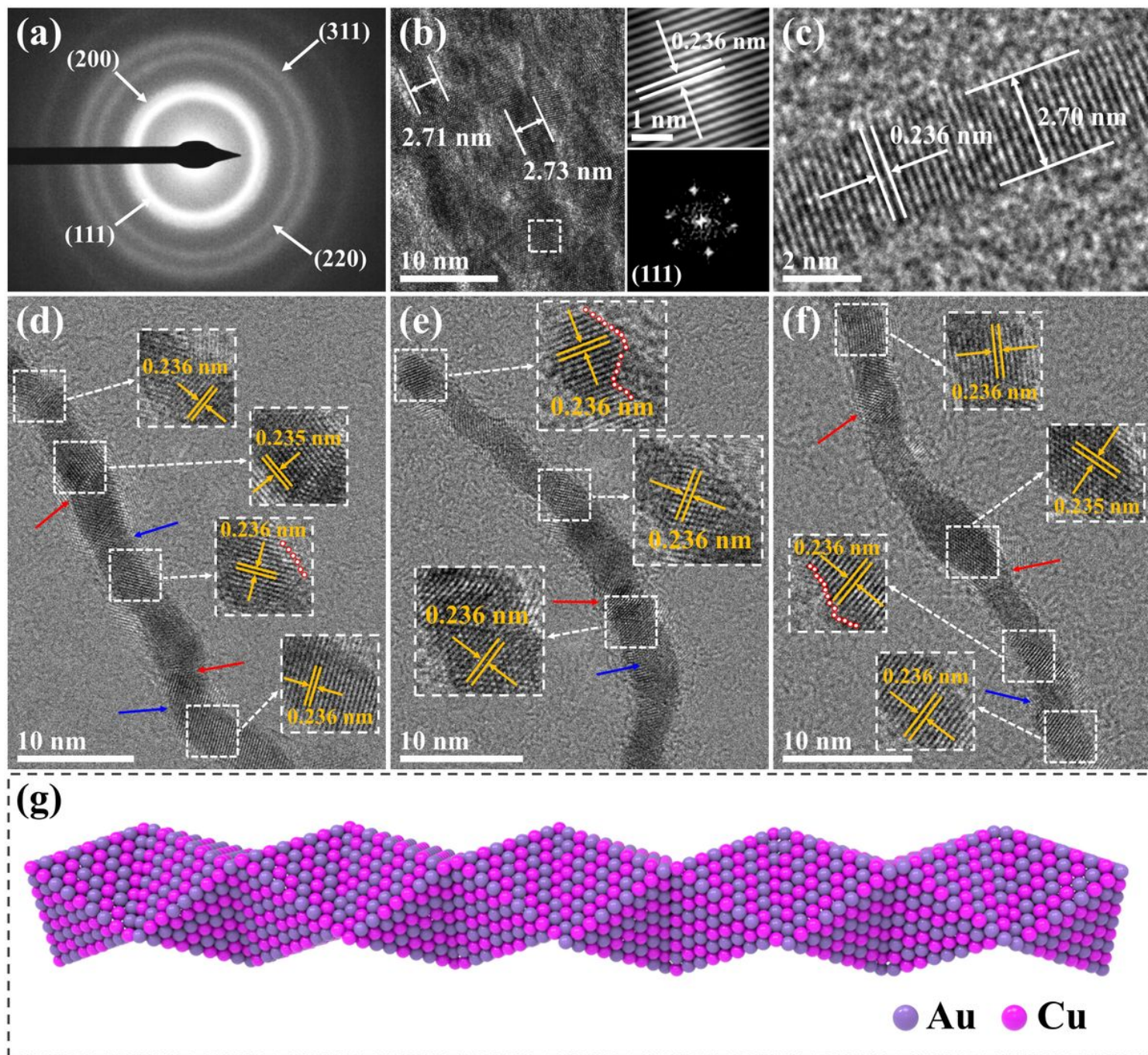


Figure 2

(a) SAED and (b) HRTEM images of the AuCu SANFs. (c-f) HRTEM images of several individual AuCu nanowire, and (g) a model illustration of the Boerdijk–Coxeter type helical nanowire. The insets in (b) display the lattice fringes of the square region and corresponding FFT pattern.

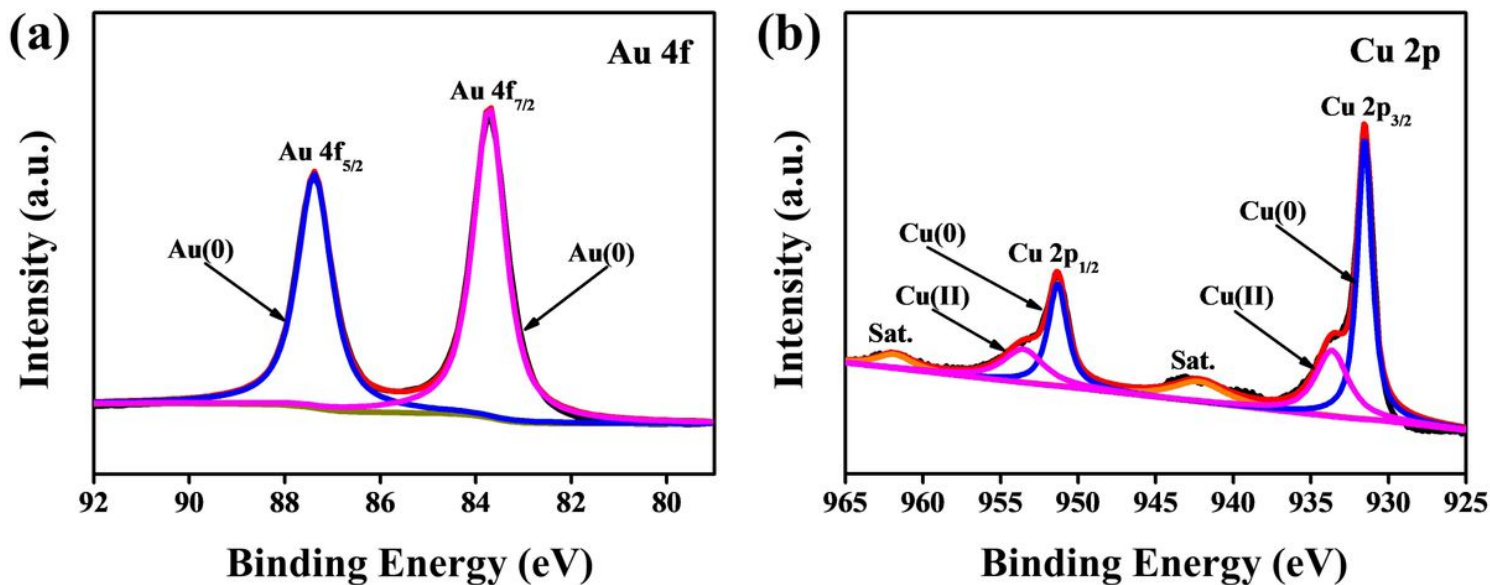


Figure 3

XPS spectra of the (a) Au 4f, and (b) Cu 2p peaks of the AuCu SANFs.

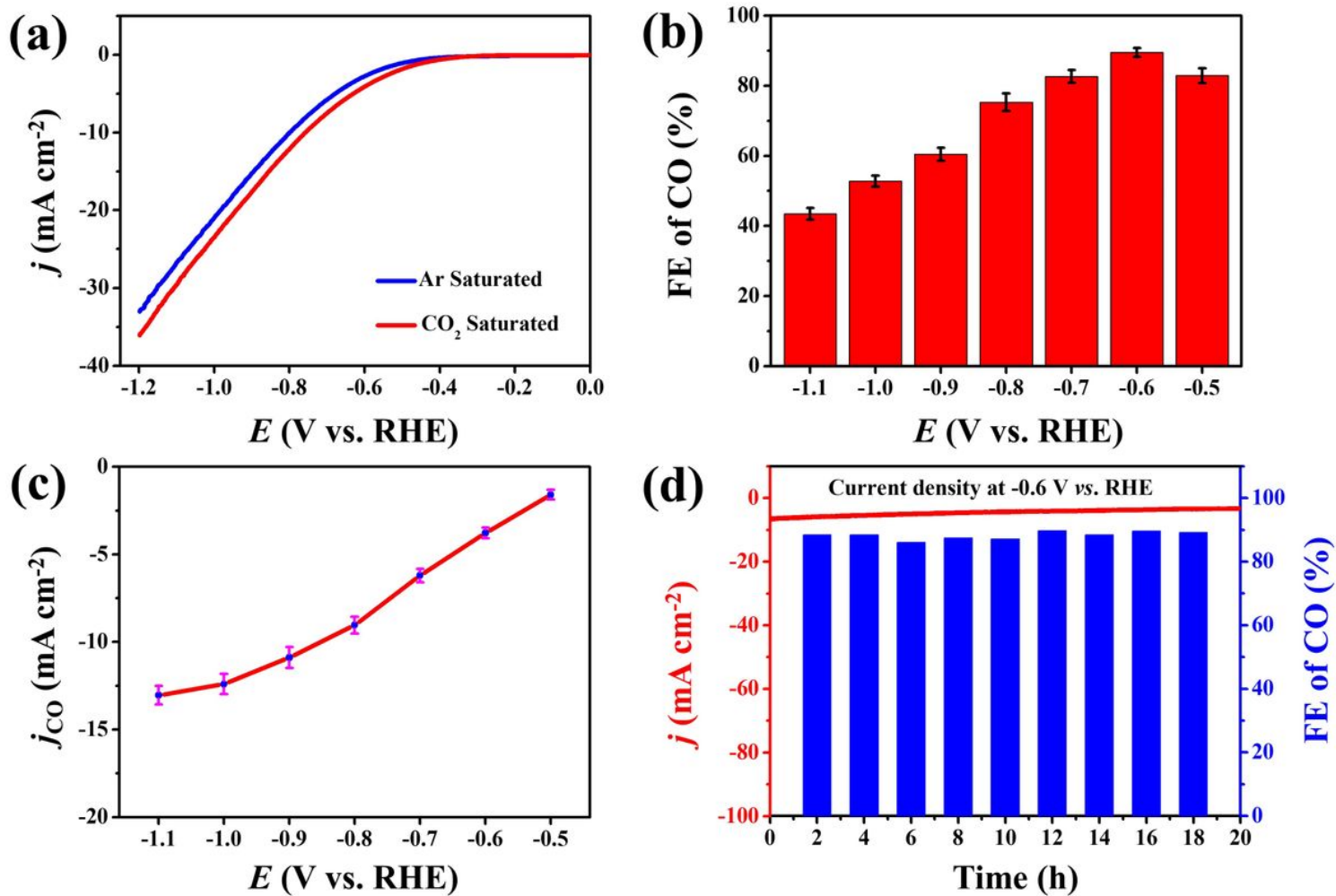


Figure 4

(a) LSV curves of the AuCu SANFs in an Ar-saturated and a CO₂-saturated 0.5 M KHCO₃ solution. (b) CO Faradaic efficiency for the AuCu SANFs examined with different applied potentials. (c) The corresponding CO partial current density. (d) The stability test conducted at -0.6 V for the AuCu SANFs.

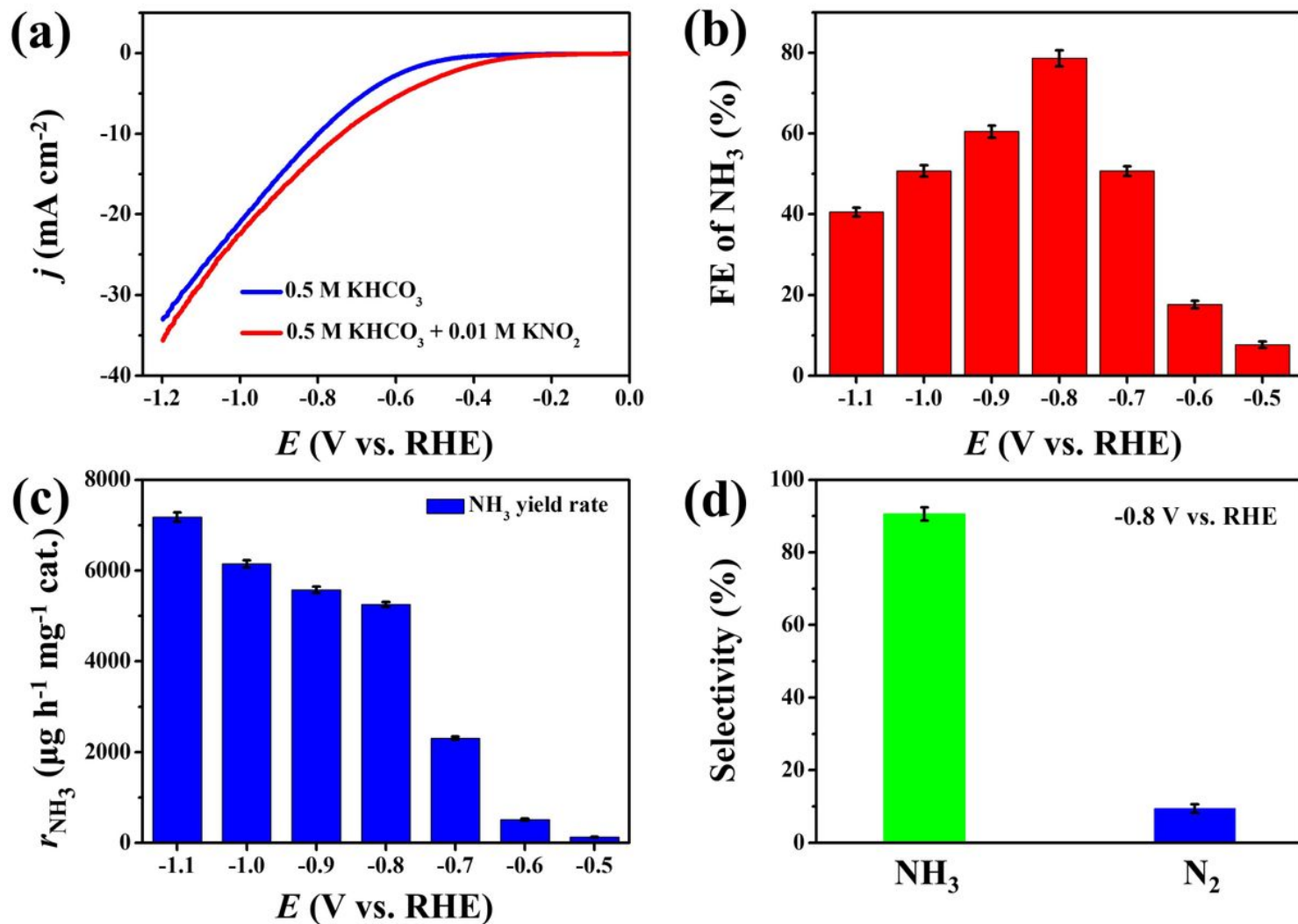


Figure 5

(a) LSV curves of the AuCu SANFs in 0.5 M KHCO₃ solution without or with 0.01 M KNO₂. (b) NH₃ Faradaic efficiency and (c) NH₃ yield rate for the AuCu SANFs examined with different applied potentials. (d) Selectivity of NH₃ and N₂ of the AuCu SANFs at -0.8 V for 2 h.

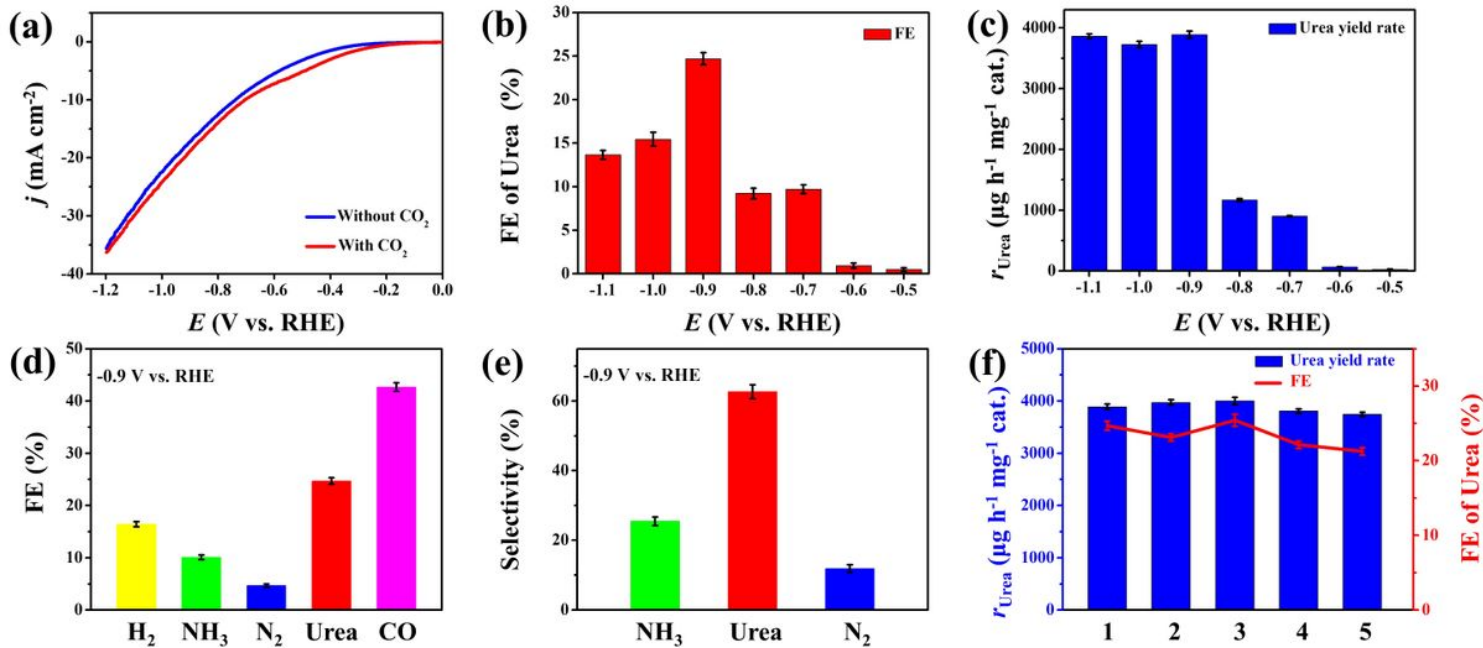


Figure 6

(a) LSV curves of the AuCu SANFs in 0.5 M KHCO₃ + 0.01 M KNO₂ solution without or with CO₂. (b) Urea Faradaic efficiency and (c) urea yield rate for the AuCu SANFs examined with different applied potentials. (d) Faradaic efficiency for different products over the AuCu SANFs at -0.9 V. (e) Selectivity of NH₃, urea and N₂ of the AuCu SANFs at -0.9 V for 2 h. (f) Urea Faradaic efficiency and yield rate over the AuCu SANFs during 5 continuous cycles.

Supplementary Files

This is a list of supplementary files associated with this preprint. Click to download.

- [SupportingInformation.doc](#)